

## Inverse Design of Plasmonic Structures with FDTD

Zhou Zeng, Prabhu K. Venuthurumilli, and Xianfan Xu\*

Cite This: <https://doi.org/10.1021/acsphotonics.1c00260>

Read Online

ACCESS |



Metrics &amp; More



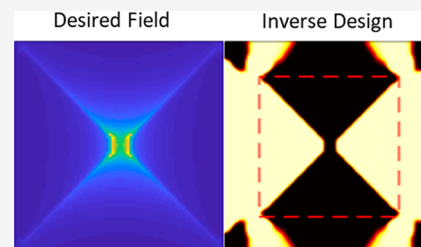
Article Recommendations



Supporting Information

**ABSTRACT:** Inverse design has greatly expanded photonic devices for achieving optimized performance. However, the use of inverse design for plasmonic structures has been challenging due to local field concentrations that can lead to errors in gradient calculation when the continuum adjoint method is used. On the other hand, with the discrete adjoint method one can achieve the exact gradient. Historically the discrete version is exclusively used with a Finite Element model, and applying the Finite-Difference Time-Domain (FDTD) method in the inverse design of plasmonic structures is rarely attempted. Due to the popularity of using FDTD in simulating plasmonic structures, we develop the discrete adjoint method with FDTD and present a framework to carry out the inverse design of plasmonic structures using density-based topology optimization. We demonstrate the exactness of the gradient calculation for a plasmonic structure with varying permittivity. Another challenge that is unique with plasmonic structures is that nonphysical amplification caused by poorly chosen material interpolation can destroy a stable convergence of the optimization. To avoid this, we adopt a nonlinear material interpolation scheme in the FDTD solver. In addition, filtering-and-projection regularization is incorporated to ensure manufacturability of the designed nanostructures. As an example of this framework, the successful reconstruction of electric fields of a plasmonic bowtie aperture is presented.

**KEYWORDS:** topology optimization, inverse design, plasmonics, FDTD, adjoint method



Plasmonics is one of the most widely studied areas in modern photonics with a wide range of applications, including super-resolution imaging,<sup>1,2</sup> nanolithography,<sup>3,4</sup> biosensing,<sup>5</sup> and high density data storage.<sup>6,7</sup> Inverse design of plasmonics has been reported in recent years<sup>8–10</sup> and is almost exclusively performed using density-based topology optimization with the Finite Element Method (FEM), where the gradient is calculated using the discrete adjoint method. In this approach, the geometry is divided into small elements of which the material property is parametrized by density parameters and the gradients of the discretized objective function with respect to the density parameters are used to evolve the solution.<sup>11</sup> The other common variation of inverse design<sup>12,13</sup> uses level-set topology optimization with FEM and the continuum adjoint method. Instead of directly associating density parameters with small elements, the level-set approach represents domains and their boundaries as level sets of a continuous function.<sup>14</sup> Also, instead of calculating gradients based on the discretized objective function, the continuum adjoint method calculates gradients based on the original continuum objective function and then evaluates it numerically.<sup>15</sup>

Up until now, topology optimization with the Finite-Difference Time-Domain (FDTD)<sup>16</sup> technique has been rare in inverse design of plasmonic structures. There are two reasons for this. First, using the continuum adjoint method with FDTD is challenging because numerical errors in electromagnetic simulations of plasmonic structures are highest at the metal–dielectric interfaces. These locations contribute

strongly to design sensitivities<sup>17</sup> and can lead to a highly inaccurate sensitivity calculation. By refining conformal boundary representation in the FEM, one can obtain highly accurate design sensitivities. However, the boundary is not conformal in FDTD and cannot be refined easily either. Second, implementing the discrete adjoint method in FDTD is more difficult than in the FEM because it does not have a direct matrix representation of the system and thus requires more customized programming. As a result, most literature uses FEM in inverse design of plasmonic structures. Due to the popularity of using FDTD in simulating plasmonics, we propose a new way to carry out the inverse design of plasmonic structures with a FDTD solver. Since plasmonics is mostly concerned with frequency-domain response, results from FDTD are first converted into a frequency domain and then analyzed. We then incorporate the frequency-domain discrete adjoint method into a density-based topology optimization framework. This method can be built upon an existing FDTD solver and accepts any differentiable frequency-domain objective function. Another challenge unique with plasmonic structures is that nonphysical field amplification can occur in and around spatial regions containing nonphysical mixtures of

Received: February 17, 2021

material densities and can destroy the stable convergence of the design procedure toward physically admissible designs.<sup>9</sup> A nonlinear material interpolation scheme is demonstrated to improve the behavior of the topology optimization compared to the linear or inverse material interpolation and is implemented in our method.

There are two original methods of sensitivity calculation of plasmonic structures with FDTD that can be used in inverse design. The adjoint variable method (AVM)<sup>18</sup> considers the time marching scheme in FDTD as a dynamic system and uses time reversal to simulate the adjoint system. This method uses the discrete adjoint method and is shown to work reasonably well for both dielectrics<sup>19</sup> and plasmonics.<sup>20</sup> However, the objective function is restricted to a time-domain integral function. It is not applicable to functions that have a nonlinear dependence on frequency-domain variables such as the optical absorption. Our method transforms the dynamic system into frequency domain and is compatible with general differentiable frequency-domain functions. The other method is based on topological derivatives<sup>21</sup> and has been applied in the design of a near-field transducer for heat-assisted magnetic recording.<sup>22</sup> It evolves a bit-map representation of structure by metalizing bits at the boundary and in the void. Each bit is either metalized or nonmetalized based on changes in the objective function due to perforation of the material domain by an infinitesimal hole. However, it calculates topological derivatives based on the original continuum governing equation and is not immune to errors caused by field concentrations.

The paper is structured as follows: We first describe the derivation of the frequency-domain discrete adjoint method with FDTD and validate its accuracy with a numerical example. Subsequently, we introduce a density-based topology optimization method that incorporates the discrete adjoint method. Filtering-and-projection regularization and the nonlinear material interpolation scheme are applied to jointly improve robustness. The method is illustrated through reconstruction of electric fields of a plasmonic bowtie aperture antenna.

## DISCRETE ADJOINT METHOD: FDTD IN FREQUENCY DOMAIN

**Derivation of the Adjoint Method.** To convert the leapfrog time-stepping scheme of FDTD into a frequency-domain matrix representation, we apply the discrete-time Fourier transform (DTFT).<sup>23</sup> We present the derivation in Supporting Information 1. In short, the joint operations of FDTD discretization and DTFT convert the original Maxwell's curl equations

$$\begin{pmatrix} -\frac{\partial}{\partial t}\epsilon^* & \nabla \times \\ \nabla \times & \frac{\partial}{\partial t}\mu^* \end{pmatrix} \begin{pmatrix} \mathbf{E} \\ \mathbf{H} \end{pmatrix} = \begin{pmatrix} \mathbf{J} \\ -\mathbf{M} \end{pmatrix} \quad (1)$$

into a frequency-domain matrix representation

$$\begin{pmatrix} -i\omega D_\epsilon(z) & \mathbf{C}_h \\ \mathbf{C}_e & i\omega D_h(z) \end{pmatrix} \begin{pmatrix} \tilde{\mathbf{e}}(z) \\ \tilde{\mathbf{h}}(z) \end{pmatrix} = \begin{pmatrix} \tilde{\mathbf{j}}(z) \\ -\tilde{\mathbf{m}}(z) \end{pmatrix} \quad (2)$$

where  $z = e^{i\omega\Delta t}$  is used for simplicity, and the tilde denotes the DTFT of the corresponding variable. Column vector  $\tilde{\mathbf{e}}(z) = (\dots, \tilde{E}_x^{i,j,k}(z), \tilde{E}_y^{i,j,k}(z), \tilde{E}_z^{i,j,k}(z), \dots)^T$  represents the transformed electric field  $\mathbf{E}$  at discretized points of Yee cells shown in

Figure 1 and  $\tilde{\mathbf{h}}(z)$ ,  $\tilde{\mathbf{j}}(z)$ , and  $\tilde{\mathbf{m}}(z)$  represent  $\mathbf{H}$ ,  $\mathbf{J}$ , and  $\mathbf{M}$ , respectively, following similar notations.  $D_\epsilon(z) = \text{diag}(\dots,$

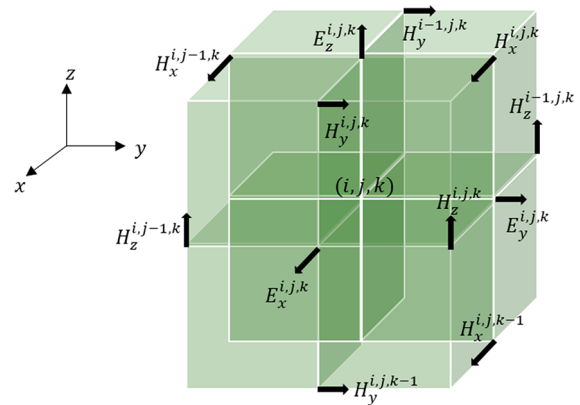


**Figure 1.** Component arrangement of the Yee cell. Each  $E$  component is surrounded by four  $H$  components and each  $H$  component is surrounded by four  $E$  components.

$\epsilon_x^{i,j,k}(z), \epsilon_y^{i,j,k}(z), \epsilon_z^{i,j,k}(z), \dots$ ) is a diagonal matrix for permittivity, and  $D_h(z) = \text{diag}(\dots, \mu_x^{i,j,k}(z), \mu_y^{i,j,k}(z), \mu_z^{i,j,k}(z), \dots)$  is a diagonal matrix for permeability. Both frequency-dependent permittivity and permeability are discretized into the  $z$ -transform space.<sup>24</sup>  $\mathbf{C}_h$  and  $\mathbf{C}_e$  are the discretized curl operators. The resulted representation is equivalent to the one of the Finite-Difference Frequency-Domain (FDFD) method<sup>25</sup> and is symmetric in an open region problem with lossy isotropic materials.

According to the adjoint method,<sup>26</sup> given an objective function  $F(\mathbf{E}(\omega), \mathbf{H}(\omega)) \in \mathbb{R}$ , which is numerically evaluated as  $f(\tilde{\mathbf{e}}(z), \tilde{\mathbf{h}}(z)) \in \mathbb{R}$ , variation of the numerical evaluation  $f$  produced by variation of material properties  $\delta D_\epsilon(z)$  and  $\delta D_h(z)$  is given by

$$\begin{aligned} \delta f &= \text{Re} \left\{ - \begin{pmatrix} \tilde{\mathbf{e}}_a(z) \\ \tilde{\mathbf{h}}_a(z) \end{pmatrix}^T \delta \begin{pmatrix} -i\omega D_\epsilon(z) & \mathbf{C}_h \\ \mathbf{C}_e & i\omega D_h(z) \end{pmatrix} \begin{pmatrix} \tilde{\mathbf{e}}(z) \\ \tilde{\mathbf{h}}(z) \end{pmatrix} \right\} \\ &= \text{Re} \left\{ - \begin{pmatrix} \tilde{\mathbf{e}}_a(z) \\ \tilde{\mathbf{h}}_a(z) \end{pmatrix}^T \begin{pmatrix} -i\omega \delta D_\epsilon(z) & \\ & i\omega \delta D_h(z) \end{pmatrix} \begin{pmatrix} \tilde{\mathbf{e}}(z) \\ \tilde{\mathbf{h}}(z) \end{pmatrix} \right\} \\ &= \text{Re} \left\{ i\omega \tilde{\mathbf{e}}_a^T(z) \delta D_\epsilon(z) \tilde{\mathbf{e}}(z) - i\omega \tilde{\mathbf{h}}_a^T(z) \delta D_h(z) \tilde{\mathbf{h}}(z) \right\} \\ &= \text{Re} \left\{ \sum_{w,i,j,k} i\omega \tilde{E}_w^{i,j,k}(z) \tilde{E}_{aw}^{i,j,k}(z) \delta \epsilon_w^{i,j,k}(z) - i\omega \tilde{H}_w^{i,j,k}(z) \tilde{H}_{aw}^{i,j,k}(z) \delta \mu_w^{i,j,k}(z) \right\} \quad (3) \end{aligned}$$

where  $(\tilde{\mathbf{e}}_a(z), \tilde{\mathbf{h}}_a(z))$  is the adjoint solution satisfying

$$\begin{pmatrix} -i\omega D_\epsilon(z) & \mathbf{C}_h \\ \mathbf{C}_e & i\omega D_h(z) \end{pmatrix} \begin{pmatrix} \tilde{\mathbf{e}}_a(z) \\ \tilde{\mathbf{h}}_a(z) \end{pmatrix} = \begin{pmatrix} \overline{\nabla_e f} \\ \overline{\nabla_h f} \end{pmatrix} \quad (4)$$

The adjoint currents  $\overline{\nabla_e f}, \overline{\nabla_h f}$  are conjugates of the first derivatives of the objective function with respect to field variables<sup>26</sup>

$$\nabla_f = \begin{pmatrix} \vdots \\ \partial f / \partial \tilde{E}_x^{i,j,k,n} \\ \partial f / \partial \tilde{E}_y^{i,j,k,n} \\ \partial f / \partial \tilde{E}_z^{i,j,k,n} \\ \vdots \end{pmatrix}, \quad \nabla_{h^*} f = \begin{pmatrix} \vdots \\ \partial f / \partial \tilde{H}_x^{i,j,k,n} \\ \partial f / \partial \tilde{H}_y^{i,j,k,n} \\ \partial f / \partial \tilde{H}_z^{i,j,k,n} \\ \vdots \end{pmatrix} \quad (5)$$

The symmetry of the system matrix suggests the same setup can be used for both forward simulation (eq 2) and adjoint simulation (eq 4), and the only difference between them is the source currents. In practice, open region problems are terminated with PMLs. The same sensitivity formula is applicable provided that PMLs are properly configured to absorb most outgoing waves. Additionally, the summation in (eq 3) is the FDTD equivalence of integration, and the Re operator comes from the fact that the objective function is real.

To solve the adjoint simulation, the objective function needs to be written explicitly with arguments from vectors  $\tilde{e}(z)$  and  $\tilde{h}(z)$  with respect to which the derivatives can be calculated to get the adjoint currents in frequency domain. In practice, the objective function is calculated based on fields linearly interpolated from the original electromagnetic fields at Yee cells. Finite-length time series signals are calculated based on the complex adjoint currents so that the adjoint simulation (eq 4) can be constructed and solved with FDTD in time domain. In essence, this is similar to designing a digital finite impulse response (FIR) filter<sup>27</sup> from a prescribed frequency domain response. We provide an implementation of adjoint currents using the frequency sampling method and a simplified version when there is only one frequency in Supporting Information 2. With solutions from the forward and the adjoint problems, sensitivity is evaluated according to eq 3.

**Example: Plasmonic Scatterer With Varying Permittivity.** We first demonstrate the accuracy of the discrete adjoint method by computing the sensitivity of the Poynting flux of a plasmonic scatterer with respect to a density parameter controlling its permittivity. To verify this sensitivity analysis, we benchmark it against the central difference method. We calculate the Poynting flux over a specified region enclosing the plasmonic scatterer.<sup>28</sup>

$$F = \int_S \text{Re}(\mathbf{E} \times \mathbf{H}) \cdot \hat{n} \, dS \quad (6)$$

We consider a simple geometry for the plasmonic scatterer, a block with a size of  $30 \times 30 \times 30 \text{ nm}^3$ . The block has spatially uniform permittivity described by a density parameter  $\rho$  using linear interpolation

$$\varepsilon(\rho) = \varepsilon_1 \rho + \varepsilon_2(1 - \rho) \quad (7)$$

where  $\varepsilon_1$  is the permittivity of gold and  $\varepsilon_2$  is the permittivity of vacuum. According to eq 3, the adjoint sensitivity is given by

$$\frac{\partial f}{\partial \rho}(\rho) = \text{Re} \left( \sum_{w,i,j,k} i\omega \tilde{E}_w^{i,j,k}(z) \tilde{E}_{aw}^{i,j,k}(z) (\varepsilon_1 - \varepsilon_2) \right) \quad (8)$$

A plane wave of wavelength 800 nm is incident upon the block. The layout for the example is shown in Figure 2. It should be noted that periodic boundary conditions are enabled on the boundaries perpendicular to the propagating direction of the

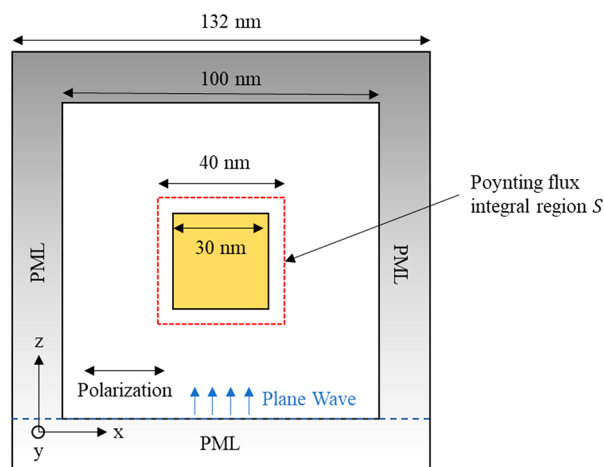


**Figure 2.** Layout for the example. A block of size  $30 \times 30 \times 30 \text{ nm}^3$  is seated in an open region with its axis aligned with coordinates. An incident plane wave travels in the  $z^+$  direction. PMLs of eight-cell thickness are used to absorb any outgoing waves. The Poynting flux is integrated on the box surrounding the block.

plane wave to mathematically produce an infinitely long source current that produces a planewave.

We take the Lorentz–Drude model<sup>29</sup> as the dispersion model of gold. We linearly scale the strength of each susceptibility to implement the linearly interpolated permittivity (eq 7). At 800 nm, the permittivity of gold is  $\varepsilon_1 = \varepsilon_0(-22.3 - 2.03j)$ , calculated from the Lorentz–Drude model. We use a 2 nm Yee cell length to run forward simulations to calculate the Poynting flux versus the density parameter  $\rho$  and run adjoint simulations to get the sensitivity with respect to  $\rho$ .

We then compare the adjoint sensitivity (eq 8) with the sensitivity calculated from a central difference scheme

$$\frac{\partial f}{\partial \rho}(\rho) \cong \frac{f(\rho + \Delta\rho) - f(\rho - \Delta\rho)}{2\Delta\rho} \quad (9)$$

to verify the accuracy of the discrete adjoint sensitivity formula. Figure 3a,b compares the two zoomed-in ranges of  $\rho$ , with  $\Delta\rho = 0.0025$ . Figure 3c,d displays the relative error of the discrete adjoint calculation against the central difference calculation. While 95% of the relative errors are less than 0.05, there are 1% of errors larger than 0.2 (see square markers in Figure 3c). They are larger than usual because their sensitivity or the denominator of the relative error is close to 0. In general, there is good agreement between the two methods, which confirms the validity of the discrete adjoint sensitivity formula.

## DENSITY-BASED TOPOLOGY OPTIMIZATION

The adjoint method calculates gradients with only two simulations, the convenience of which makes gradient-based optimizations that involve millions of variables possible, for example, permittivity at each discretized location. The density-based topology optimization is one of many gradient-based optimizations that is extensively used in inverse design of photonic devices.<sup>8–10,30–36</sup> It represents the design using a vector  $\rho$  of continuous density parameters  $\rho^i \in [0,1]$  that are mapped to the physical material distribution by a material interpolation scheme and utilizes the adjoint method to obtain gradients. For example, we can assign value to a permittivity  $\varepsilon^i(z)$  in FDTD using linear interpolation

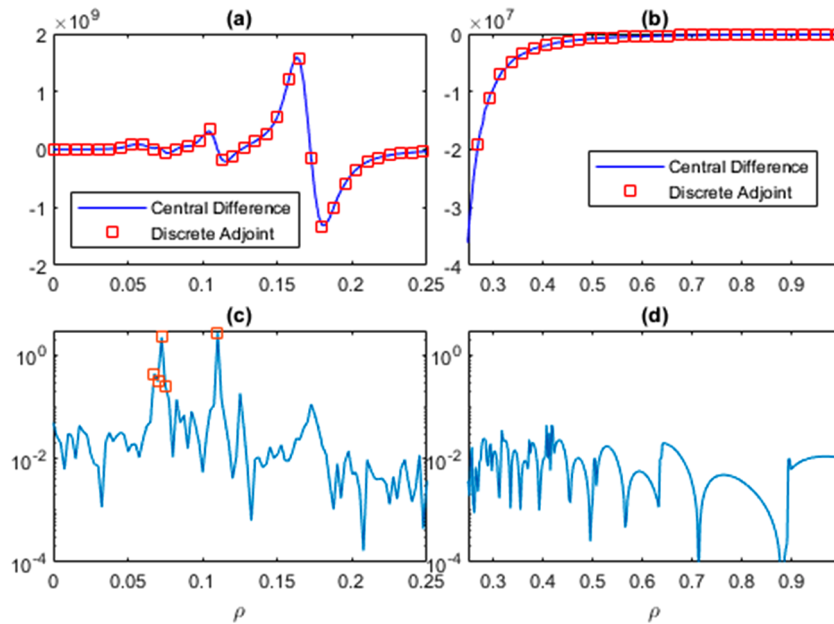


**Figure 3.** (a, b) Comparison of the central difference sensitivity and the discrete adjoint sensitivity. (c, d) Relative error of the discrete adjoint calculated by  $\delta(\rho) = |f'_{\text{discrete adjoint}} - f'_{\text{central difference}}|/|f'_{\text{central difference}}|$ ; points marked in squares are values larger than 0.2.

$$\varepsilon^i(\rho^i, z) = \varepsilon_1(z)\rho^i + \varepsilon_2(z)(1 - \rho^i) \quad (10)$$

where  $\varepsilon_1$  is the permittivity for the material domain and  $\varepsilon_2$  is the permittivity for the void domain (usually  $\varepsilon_2 = \varepsilon_0$ ). In our approach, a rectangular design domain is constructed with a regular grid (Cartesian lattice). Each point in the grid is assigned a density parameter  $\rho^i$  and linear interpolation is used to map grid density parameters into Yee lattice density parameters, which then determines the material property by the linear material interpolation.

It is also demonstrated<sup>9</sup> that in the topology optimization of plasmonics, the linear interpolation in eq 10 can cause nonphysical field amplification. Such amplification is unique for problems that involve negative permittivity, for example, plasmonic materials, and destroys the stable convergence of the optimization. A nonlinear material interpolation scheme is introduced<sup>9</sup> to improve the convergence behavior and hence incorporated into our method. In the nonlinear method, the refractive index is linearly interpolated:

$$\begin{aligned} \varepsilon^i(\rho^i, z) &= (\rho^i \sqrt{\varepsilon_1(z)} + (1 - \rho^i) \sqrt{\varepsilon_2(z)})^2 \\ &= \rho^2 \varepsilon_1(z) + (1 - \rho^i)^2 \varepsilon_2(z) + 2\rho^i(1 - \rho^i) \sqrt{\varepsilon_1(z)\varepsilon_2(z)} \end{aligned} \quad (11)$$

In contrast to FEM, there is no direct way of implementing the nonlinear interpolation in FDTD since  $\sqrt{\varepsilon_1(z)\varepsilon_2(z)}$  is not a rational function in general. We construct a rational function  $\varepsilon_3(z)$  to approximate  $\sqrt{\varepsilon_1(z)\varepsilon_2(z)}$  in the frequency range that the objective function concerns. On the other hand, an approximation is good enough, as eq 11 is a valid material interpolation irrelevant of  $\varepsilon_3(z)$ . Constructing a rational approximation is the same as designing an infinite impulse response (IIR) filter<sup>27</sup> by a prescribed frequency domain response. Supporting Information 3 details the implementation of nonlinear material interpolation in FDTD using the vector fitting technique<sup>37</sup> that also guarantees stability of the filter.

The three-field density representation<sup>38</sup> is adopted as the regularization technique in our method to remove very small

features to ensure manufacturability, which uses a density filter followed by a projection. Each density value  $\rho^i$  is reassigned as a weighted sum of its neighbors:

$$\hat{\rho}^i = \frac{\sum_{j \in N_i} w_{ij} \rho^j}{\sum_{j \in N_i} w_{ij}} \quad (12)$$

We use a Gaussian distribution function<sup>39</sup> for the filter function  $w_{ij}$

$$w_{ij} = e^{-0.5(x_i - x_j/R)^2} \quad (13)$$

where  $R$  denotes the filter radius which is used to truncate the filter and is deemed as the minimum feature size of the design. Density filters can effectively remove small features during the optimization process but can end up creating more gray transition regions. Therefore, a projection operator is used to project the filtered density to 0/1. The following projection operator<sup>40</sup> is used in our method:

$$\bar{\rho}^i = \frac{\tanh(\beta\eta) + \tanh(\beta(\hat{\rho}^i - \eta))}{\tanh(\beta\eta) + \tanh(\beta(1 - \eta))} \quad (14)$$

where  $\beta$  is a parameter used to control the strength of the projection and  $\eta \in [0, 1]$  defines the projection level. Eventually, projected density parameters  $\bar{\rho}^i$  are used as the actual density in the simulation. To prevent the optimization from getting stuck in local minimum earlier in the process due to the density being projected to 0/1 immediately, projection strength  $\beta$  is increased after the objective function has not changed much after a certain number of iterations,  $n_{sc}$ , mimicking the  $\beta$ -continuation scheme.<sup>40</sup>

We programmed a FDTD solver in C++ for handling solutions of forward and adjoint problems. The solver allows specifying material property of each Yee cell point so that we are able implement the nonlinear material interpolation. A Python interface was designed to communicate to the solver, calculate sensitivities, and evolve solutions in each inner iteration using the method of moving asymptotes (MMA).<sup>41</sup>

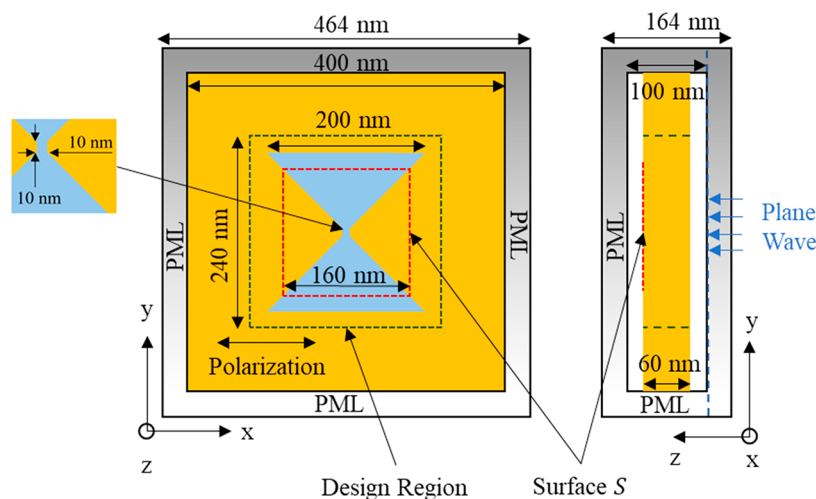


**Figure 4.** Layout for the optimization. All rectangles are squares with their centers aligned. An incident wave of wavelength 800 nm is traveling in direction perpendicular to the gold layer marked in yellow.

The overall flow diagram for the density-based topology optimization with the discrete adjoint sensitivity formula is provided in Supporting Information 2.

### CASE STUDY: RECONSTRUCTION OF ELECTRIC FIELDS OF A PLASMONIC BOWTIE APERTURE

Plasmonic bowtie apertures are known to produce highly localized fields and have potential applications including optical lithography<sup>4</sup> and high density data storage.<sup>42</sup> The enhanced electric fields are confined within only a region of the nanometer length scale near the surface of the nanostructures and decay significantly thereafter.<sup>43</sup> In this example, reconstruction of the electric fields of a plasmonic bowtie aperture is carried out to exemplify the inverse design with a nonlinear frequency-domain objective function. The reconstruction is realized by minimizing an objective function that measures the difference between the design electric field  $\mathbf{E}$  and the objective electric field  $\mathbf{E}_0$  produced by the plasmonic bowtie aperture. In other words, the objective function is defined as the normalized difference:

$$F(\mathbf{E}) = \int_S (\|\mathbf{E}\| - \|\mathbf{E}_0\|)^2 dS / \int_S \|\mathbf{E}_0\|^2 dS \quad (15)$$

where  $S$  is chosen as the exit plane of the bowtie structure. The layout for the optimization and target geometry is shown in Figure 4. The Yee cell length is 2 nm to accurately capture the near field.<sup>44</sup> The optimization follows the steps discussed in Density-Based Topology Optimization and uses a  $N_x \times N_y \times N_z$  rectangular grid for design density. Table 1 lists the parameters used in this optimization. We enforce the density to be constant along the  $z$  direction so that the optimization produces a planar structure. The optimization algorithm starts with  $\rho = 1$  and runs for five iterations in the outer loop, which constitutes a total of 60 adjoint simulations and 105 forward simulations.

The objective function in the final design is evaluated as 0.0046, suggesting a successful recovery of the electric field on the surface  $S$ , as shown in Figure 5. Although symmetry is not enforced during the optimization, the density distributions are symmetric with the same bowtie structure within the surface  $S$  region. The features at the corners of the final design are artifacts of the optimization and do not influence the centered

**Table 1.** Parameters Used in Optimization<sup>a</sup>

| parameter [unit] | value        |
|------------------|--------------|
| $R$ [nm]         | 8            |
| $\beta$          | 1            |
| $k$              | 5            |
| $\alpha$         | 0.01         |
| $c_r$            | 1.0          |
| $c_\beta$        | 1.8          |
| $N_x, N_y, N_z$  | 121, 121, 31 |
| $n_{sc}$         | 3            |

<sup>a</sup>Note that  $N_z$  discretized points are equivalent to  $N_z - 1$  discretized intervals. Please refer to the flow diagram in Supporting Information 2 for definitions of  $k$ ,  $\alpha$ ,  $c_r$ , and  $c_\beta$ .

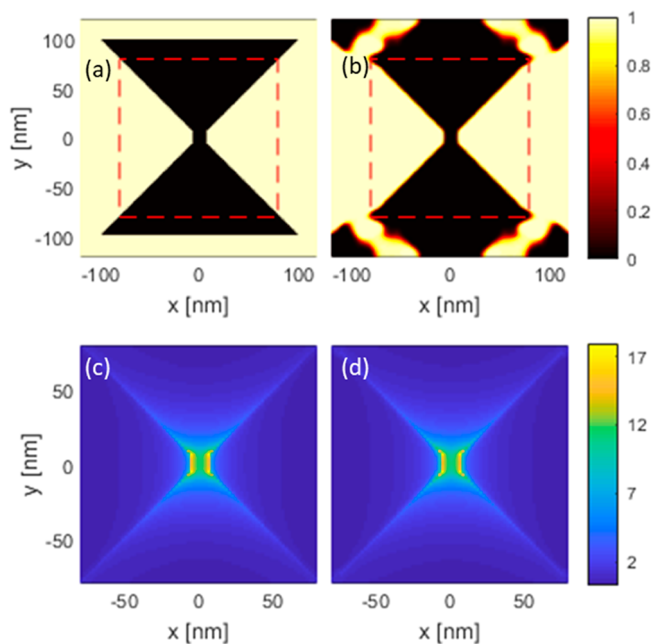


**Figure 5.** Density distribution of the original bowtie structure (a) and the final design structure (b) overlaid with surface  $S$  marked by red dashed line and their respective electric fields distribution on surface  $S$  (c, d). The electric fields distribution is normalized by incident wave intensity.

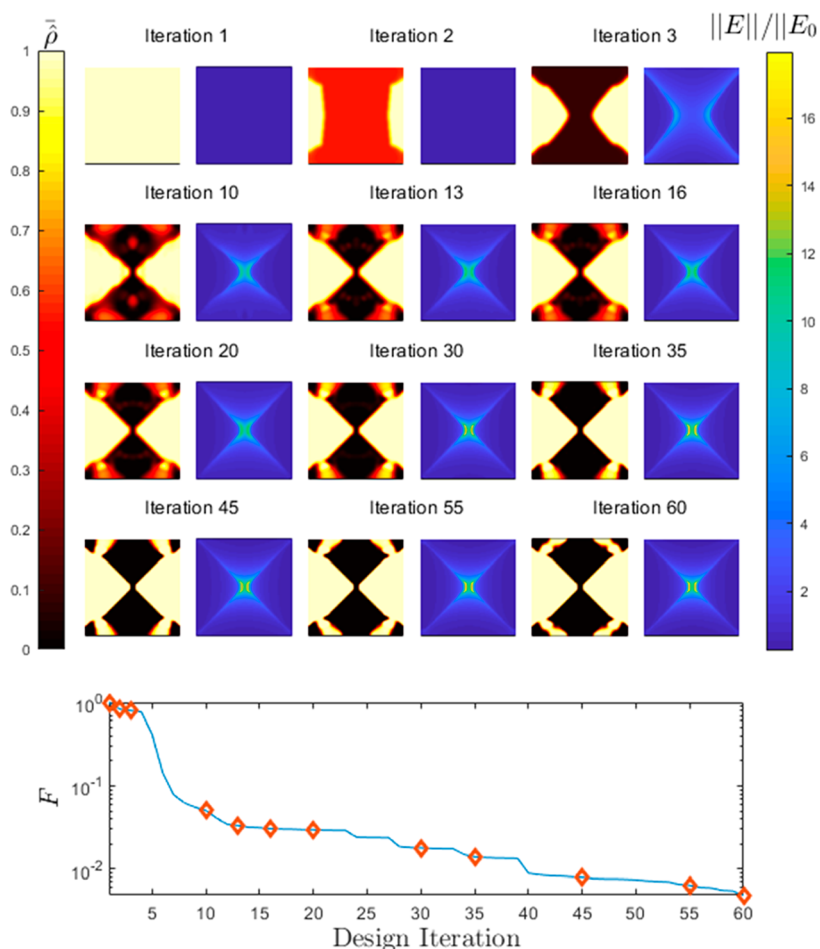


**Figure 6.** Distributions of the projected density  $\bar{\rho}^i$  (left) and the field magnitude (right) in some intermediate steps showing the evolution of the density. Each iteration is marked with a diamond in the objective function graph at the bottom. The objective function is normalized so that it is evaluated as 1 in the first iteration.

fields, as they are almost identical for the original and optimization generated designs shown in Figure 5c,d.

Figure 6 shows intermediate iterations during the optimization. The sharp decreases in the objective function happen at the beginning of each iteration in the outer loop when the projection level  $\beta$  increases. Higher value of  $\beta$  brings in higher contrast of vacuum and gold to the boundary, which contributes to the generation of highly localized fields. During the early iterations, the general shape of the final design already emerges. Early emergence of a clearly defined shape has also been reported<sup>9,43</sup> using density-based topology optimization.

## CONCLUSION

We present a method for carrying out inverse design of plasmonic structures using FDTD that incorporates the discrete adjoint method in frequency domain. This method can be built upon any existing FDTD program and accepts general differentiable objective functions. We provide detailed derivations of the adjoint method and validate it with a numerical example involving a plasmonic scatterer. The adjoint sensitivities match very well with sensitivities obtained with the central-difference scheme. Based on the discrete adjoint method, we develop a density-based topology optimization framework and improve the robustness by using the filtering-and-projection regularization and the nonlinear material interpolation. For illustration purposes, we use the method

to successfully reconstruct electric fields of a bowtie plasmonic structure.

## ASSOCIATED CONTENT

### Supporting Information

The Supporting Information is available free of charge at <https://pubs.acs.org/doi/10.1021/acsphotonics.1c00260>.

Derivation of the discrete adjoint method with FDTD in the frequency domain, implementation of the discrete adjoint method, and implementation of the nonlinear material interpolation (PDF)

## AUTHOR INFORMATION

### Corresponding Author

Xianfan Xu – School of Mechanical Engineering and Birck Nanotechnology Center, Purdue University, West Lafayette, Indiana 47906, United States; [orcid.org/0000-0003-0580-4625](https://orcid.org/0000-0003-0580-4625); Email: [xxu@ecn.purdue.edu](mailto:xxu@ecn.purdue.edu)

### Authors

Zhou Zeng – School of Mechanical Engineering and Birck Nanotechnology Center, Purdue University, West Lafayette, Indiana 47906, United States

Prabhu K. Venuthurumilli – School of Mechanical Engineering and Birck Nanotechnology Center, Purdue University, West Lafayette, Indiana 47906, United States

Complete contact information is available at:  
<https://pubs.acs.org/10.1021/acsp Photonics.1c00260>

## Notes

The authors declare no competing financial interest.

## ACKNOWLEDGMENTS

Support for this work by ASTC – the Advanced Storage Technology Consortium and the National Science Foundation (CBET-1804377) is acknowledged.

## REFERENCES

- (1) Kawata, S.; Inouye, Y.; Verma, P. Plasmonics for Near-Field Nano-Imaging and Superlensing. *Nat. Photonics* **2009**, *3* (7), 388–394.
- (2) Willets, K. A.; Wilson, A. J.; Sundaresan, V.; Joshi, P. B. Super-Resolution Imaging and Plasmonics. *Chem. Rev.* **2017**, *117* (11), 7538–7582.
- (3) Srituravanich, W.; Fang, N.; Sun, C.; Luo, Q.; Zhang, X. Plasmonic Nanolithography. *Nano Lett.* **2004**, *4* (6), 1085–1088.
- (4) Wen, X.; Datta, A.; Traverso, L. M.; Pan, L.; Xu, X.; Moon, E. E. High Throughput Optical Lithography by Scanning a Massive Array of Bowtie Aperture Antennas at Near-Field. *Sci. Rep.* **2015**, *5* (1), 16192.
- (5) Anker, J. N.; Hall, W. P.; Lyandres, O.; Shah, N. C.; Zhao, J.; Van Duyne, R. P. Biosensing with Plasmonic Nanosensors. *Nanosci. Technol.* **2009**, 308–319.
- (6) Challenger, W. A.; Peng, C.; Itagi, A. V.; Karns, D.; Peng, W.; Peng, Y.; Yang, X.; Zhu, X.; Gokemeijer, N. J.; Hsia, Y.-T.; Ju, G.; Rottmayer, R. E.; Seigler, M. A.; Gage, E. C. Heat-Assisted Magnetic Recording by a near-Field Transducer with Efficient Optical Energy Transfer. *Nat. Photonics* **2009**, *3* (4), 220–224.
- (7) Stipe, B. C.; Strand, T. C.; Poon, C. C.; Balamane, H.; Boone, T. D.; Katine, J. A.; Li, J.-L.; Rawat, V.; Nemoto, H.; Hirotsune, A.; Hellwig, O.; Ruiz, R.; Dobisz, E.; Kercher, D. S.; Robertson, N.; Albrecht, T. R.; Terris, B. D. Magnetic Recording at 1.5 Pb M–2 Using an Integrated Plasmonic Antenna. *Nat. Photonics* **2010**, *4* (7), 484–488.
- (8) Andkjær, J.; Nishiwaki, S.; Nomura, T.; Sigmund, O. Topology Optimization of Grating Couplers for the Efficient Excitation of Surface Plasmons. *J. Opt. Soc. Am. B* **2010**, *27* (9), 1828.
- (9) Christiansen, R. E.; Vester-Petersen, J.; Madsen, S. P.; Sigmund, O. A Non-Linear Material Interpolation for Design of Metallic Nano-Particles Using Topology Optimization. *Comput. Methods Appl. Mech. Eng.* **2019**, *343*, 23–39.
- (10) Wadbro, E.; Engström, C. Topology and Shape Optimization of Plasmonic Nano-Antennas. *Comput. Methods Appl. Mech. Eng.* **2015**, *293*, 155–169.
- (11) Jensen, J. S.; Sigmund, O. Topology Optimization for Nano-Photonics. *Laser Photon. Rev.* **2011**, *5* (2), 308–321.
- (12) Zhou, S.; Li, W.; Li, Q. Level-Set Based Topology Optimization for Electromagnetic Dipole Antenna Design. *J. Comput. Phys.* **2010**, *229* (19), 6915–6930.
- (13) Yamasaki, S.; Nomura, T.; Kawamoto, A.; Sato, K.; Nishiwaki, S. A Level Set-Based Topology Optimization Method Targeting Metallic Waveguide Design Problems. *Int. J. Numer. Methods Eng.* **2011**, *87* (9), 844–868.
- (14) Burger, M. A Framework for the Construction of Level Set Methods for Shape Optimization and Reconstruction. *Interfaces Free Boundaries* **2003**, *5* (3), 301–329.
- (15) van Keulen, F.; Haftka, R. T.; Kim, N. H. Review of Options for Structural Design Sensitivity Analysis. Part I: Linear Systems. *Comput. Methods Appl. Mech. Eng.* **2005**, *194* (30–33), 3213–3243.
- (16) Taflove, A.; Hagness, S. C. *Computational Electromagnetics: The Finite-Difference Time-Domain Method*; Artech House: Boston, 2000.
- (17) Hansen, P.; Hesselink, L. Accurate Adjoint Design Sensitivities for Nano Metal Optics. *Opt. Express* **2015**, *23* (18), 23899.
- (18) Nikolova, N. K.; Tam, H. W.; Bakr, M. H. Sensitivity Analysis With the FDTD Method on Structured Grids. *IEEE Trans. Microwave Theory Tech.* **2004**, *52* (4), 1207–1216.
- (19) Swillam, M. A.; Bakr, M. H.; Nikolova, N. K.; Li, X. Adjoint Sensitivity Analysis of Dielectric Discontinuities Using FDTD. *Electromagnetics* **2007**, *27* (2–3), 123–140.
- (20) Zhang, Y.; Ahmed, O. S.; Bakr, M. H. Adjoint Sensitivity Analysis of Plasmonic Structures Using the FDTD Method. *Opt. Lett.* **2014**, *39* (10), 3002.
- (21) Garreau, S.; Guillaume, P.; Masmoudi, M. The Topological Asymptotic for PDE Systems: The Elasticity Case. *SIAM J. Control Optim.* **2001**, *39* (6), 1756–1778.
- (22) Bhargava, S.; Yablonovitch, E. Lowering HAMR Near-Field Transducer Temperature via Inverse Electromagnetic Design. *IEEE Trans. Magn.* **2015**, *51* (4), 1–7.
- (23) Oppenheim, A. V.; Schaffer, R. W. *Discrete-Time Signal Processing*; Pearson Prentice Hall, 2002; pp 48–54.
- (24) Weedon, W.; Rappaport, C. M. A General Method for FDTD Modeling of Wave Propagation in Arbitrary Frequency-Dispersive Media. *IEEE Trans. Antennas Propag.* **1997**, *45* (3), 401–410.
- (25) Champagne, N. J.; Berryman, J. G.; Buettnner, H. M. FDFD: A 3D Finite-Difference Frequency-Domain Code for Electromagnetic Induction Tomography. *J. Comput. Phys.* **2001**, *170* (2), 830–848.
- (26) Tortorelli, D. A.; Michaleris, P. Design Sensitivity Analysis: Overview and Review. *Inverse Probl. Eng.* **1994**, *1* (1), 71–105.
- (27) Proakis, J. G.; Manolakis, D. G. *Digital Signal Processing: Principles, Algorithms and Applications*; Pearson Prentice Hall, 2007.
- (28) Bohren, C. F.; Huffman, D. R. *Absorption and Scattering of Light by Small Particles*; Wiley, 1998; DOI: 10.1002/9783527618156.
- (29) Rakić, A. D.; Djurišić, A. B.; Elazar, J. M.; Majewski, M. L. Optical Properties of Metallic Films for Vertical-Cavity Optoelectronic Devices. *Appl. Opt.* **1998**, *37* (22), 5271.
- (30) Lu, J.; Boyd, S.; Vučković, J. Inverse Design of a Three-Dimensional Nanophotonic Resonator. *Opt. Express* **2011**, *19* (11), 10563.
- (31) Men, H.; Nguyen, N. C.; Freund, R. M.; Parrilo, P. A.; Paire, J. Bandgap Optimization of Two-Dimensional Photonic Crystals Using Semidefinite Programming and Subspace Methods. *J. Comput. Phys.* **2010**, *229* (10), 3706–3725.
- (32) Hassan, E.; Wadbro, E.; Berggren, M. Topology Optimization of Metallic Antennas. *IEEE Trans. Antennas Propag.* **2014**, *62* (5), 2488–2500.
- (33) Kiziltas, G.; Psychoudakis, D.; Volakis, J. L.; Kikuchi, N. Topology Design Optimization of Dielectric Substrates for Bandwidth Improvement of a Patch Antenna. *IEEE Trans. Antennas Propag.* **2003**, *51* (10), 2732–2743.
- (34) Deng, Y.; Liu, Z.; Song, C.; Hao, P.; Wu, Y.; Liu, Y.; Korvink, J. G. Topology Optimization of Metal Nanostructures for Localized Surface Plasmon Resonances. *Struct. Multidiscip. Optim.* **2016**, *53* (5), 967–972.
- (35) Dyck, D. N.; Lowther, D. A. Automated Design of Magnetic Devices by Optimizing Material Distribution. *IEEE Trans. Magn.* **1996**, *32* (3), 1188–1193.
- (36) Deng, Y.; Korvink, J. G. Topology Optimization for Three-Dimensional Electromagnetic Waves Using an Edge Element-Based Finite-Element Method. *Proc. R. Soc. London, Ser. A* **2016**, *472* (2189), 20150835.
- (37) Gustavsen, B.; Semlyen, A. Rational Approximation of Frequency Domain Responses by Vector Fitting. *IEEE Trans. Power Delivery* **1999**, *14* (3), 1052–1061.
- (38) Lazarov, B. S.; Wang, F.; Sigmund, O. Length Scale and Manufacturability in Density-Based Topology Optimization. *Arch. Appl. Mech.* **2016**, *86* (1–2), 189–218.
- (39) Bruns, T. E.; Tortorelli, D. A. An Element Removal and Reintroduction Strategy for the Topology Optimization of Structures

and Compliant Mechanisms. *Int. J. Numer. Methods Eng.* **2003**, *57* (10), 1413–1430.

(40) Wang, F.; Lazarov, B. S.; Sigmund, O. On Projection Methods, Convergence and Robust Formulations in Topology Optimization. *Struct. Multidiscip. Optim.* **2011**, *43* (6), 767–784.

(41) Svanberg, K. The Method of Moving Asymptotes—a New Method for Structural Optimization. *Int. J. Numer. Methods Eng.* **1987**, *24* (2), 359–373.

(42) Betzig, E.; Trautman, J. K.; Wolfe, R.; Gyorgy, E. M.; Finn, P. L.; Kryder, M. H.; Chang, C.-H. Near-field Magneto-optics and High Density Data Storage. *Appl. Phys. Lett.* **1992**, *61* (2), 142–144.

(43) Deng, Y.; Liu, Z.; Song, C.; Wu, J.; Liu, Y.; Wu, Y. Topology Optimization-Based Computational Design Methodology for Surface Plasmon Polaritons. *Plasmonics* **2015**, *10* (3), 569–583.

(44) Lesina, A. C.; Vaccari, A.; Berini, P.; Ramunno, L. On the Convergence and Accuracy of the FDTD Method for Nanoplasmonics. *Opt. Express* **2015**, *23* (8), 10481.